Journal of Petroleum Science and Engineering 196 (2021) 107669

Contents lists available at ScienceDirect

Journal of Petroleum Science and Engineering

journal homepage: http://www.elsevier.com/locate/petrol

Simulation of fluid flow through real microannuli geometries

Anisa Noor Corina [a], Ragnhild Skorpa [b], Sigbjørn Sangesland [a], Torbjørn Vrålstad [b,*]

[a] Norwegian University of Science and Technology (NTNU), Trondheim, Norway
[b] SINTEF Industry, Trondheim, Norway

ARTICLE INFO

Keywords:
Cement microannuli
Computational fluid dynamics (CFD)
Non-linear fluid flow

ABSTRACT

Debonding of well cement towards casing or rock, i.e. microannuli formation, is a typical failure mode of cement barriers. Consequently, such microannuli may act as leak paths during leakages of downhole fluids such as hydrocarbons or CO_2. Current leakage models usually assume that microannuli have uniform geometries with homogeneous apertures, which results in linear Darcy flow. However, several recent studies have shown that microannuli do not have uniform geometries and subsequently, fluid flow through real microannuli is complex and non-linear.

This paper presents results of CFD simulations of fluid flow through real microannuli geometries, where the microannuli were experimentally created and visualized in 3D by X-ray computed tomography (CT). Simulations were performed with three different fluids of varying viscosity and density – methane gas, liquid water, and liquid oil. The results visualize how the non-uniform flow path geometry and surface roughness of real microannuli create tortuous flow patterns, especially locally around bottlenecks and other heterogeneities. It is also seen that these complex flow patterns result in non-linear dependencies between flow rate and pressure difference for the less viscous fluids, i.e. gas and water, whereas the more viscous oil display linear flow.

1. Introduction

Throughout the life cycle of a well, the integrity of well barriers must be maintained to prevent uncontrolled flow of downhole fluids to the surface, freshwater aquifers, or surrounding formations. Some wells experience well barrier failures however (Bourgoyne et al., 1999; Vignes and Aadnoy, 2010), and for example, considerable methane leakages have been found for several plugged wells after well abandonment (Watson and Bachu, 2009; Trudel et al., 2019).

Cement is an important well barrier material, and during well construction, cement slurry is placed in the annulus between the formations and the casing strings to provide zonal isolation (Nelson and Guillot, 2006). Good cement typically have gas permeability in the order of 10 μD (Oil & Gas UK, 2015) and water permeability in the order 0.01 μD or less (Bachu and Bennion, 2009), and thus provides a good sealing towards downhole fluids. However, defects could form in the cement sheath from several mechanisms, such as shrinkage and exposure to temperature and pressure variations during normal production operations (Bois et al., 2011; Nygaard et al., 2014; Therond et al., 2017). Typical such defects are microannuli, i.e. when there is no or poor bonding between the cement and the surrounding casing or formation. The presence of such cement sheath debonding might increase the effective wellbore permeability (Duguid et al., 2013; Gasda et al., 2013). Furthermore, microannuli may also form around cement plugs which are placed in the wellbore after well abandonment (Nagelhout et al., 2010; Vrålstad et al., 2019; Corina et al., 2020).

In most cases, such microannuli represent a potential leakage pathway for downhole fluids. In this regard, it is important to note the difference between *cement mechanical integrity* and *cement hydraulic integrity* (Bois et al., 2019), where mechanical integrity is the potential presence of cracks and microannuli, and hydraulic integrity is the resulting flow rates through these defects in the cement barrier. With respect to zonal isolation, the hydraulic integrity is what matters, and it is thus of importance to study and understand flow of downhole fluids through microannuli. For example, a good understanding of microannuli flow is essential when predicting potential future leak rates from plugged and abandoned wells (Vrålstad et al., 2019). However, in several model predictions (e.g. Moeinikia et al., 2018; Ford et al., 2018), it often assumed that microannuli geometries are homogeneous with uniform apertures, where the resulting fluid flow follows linear correlations. Moreover, several experimental studies of fluid flow though microannuli assume such uniformity and estimate “equivalent” or “effective”

* Corresponding author.
E-mail address: torbjorn.vralstad@sintef.no (T. Vrålstad).

https://doi.org/10.1016/j.petrol.2020.107669
Received 6 July 2020; Accepted 17 July 2020
Available online 21 July 2020

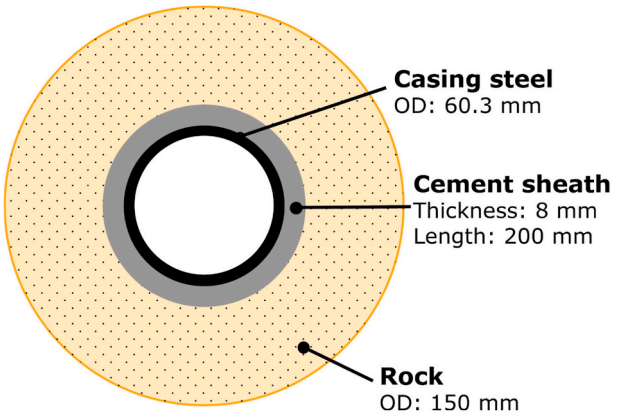

Fig. 1. The cross-section of the configuration for the cement sheath samples.

microannuli sizes based on the measured flow rates (Boukhelifa et al., 2004; Nagelhout et al., 2010; Aas et al., 2016).

Despite the merits and convenience of assuming microannuli uniformity, several experimental studies have shown that this approach is too simplified. For example, X-ray computed tomography (CT) visualizations of experimentally created cement microannuli have shown that microannuli geometries are not uniform or homogeneous (De Andrade et al., 2014, 2016; Vrålstad et al., 2019). Real microannuli have fracture-like and complex geometries with non-uniform apertures, and do not always form around the entire circumference of the cement. Furthermore, Skorpa and Vrålstad (2018) used one of these experimentally created microannuli as imported flow path geometry in computational fluid dynamics (CFD) simulations and found that gas flow thorough real microannuli can be complex and non-linear. Recently, Stormont and co-workers performed several experiments where they studied gas flow through different microannuli sizes (Stormont et al., 2018; Garcia et al., 2019; Hatambeigi et al., 2020). They found that the measured gas flow rates through these experimentally created microannuli did not follow linear flow behaviour. Moreover, they also found

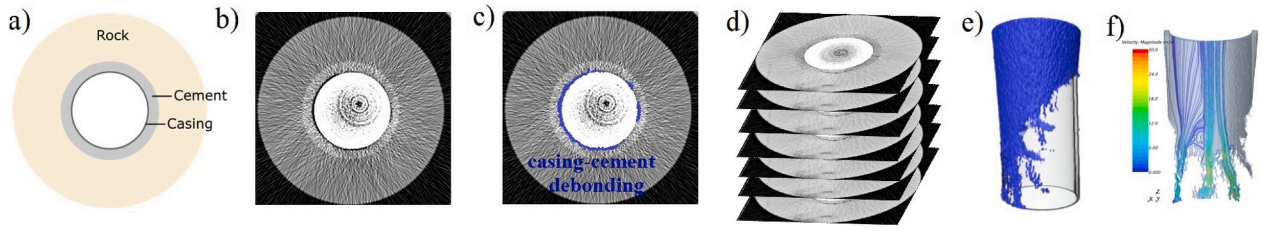

Fig. 2. The process of extracting microannuli geometries from experimental samples by using X-ray CT: (a) Illustration of sample cross-section. (b) A 2D CT image showing defects in the cement sheath. (c) Segmentation of defects at cement-casing interface. (d) The stack of 2D CT images assembled into a 3D volume. (e) The final 3D volume of cement microannulus. f) Microannulus imported into CFD tool as flow path geometry.

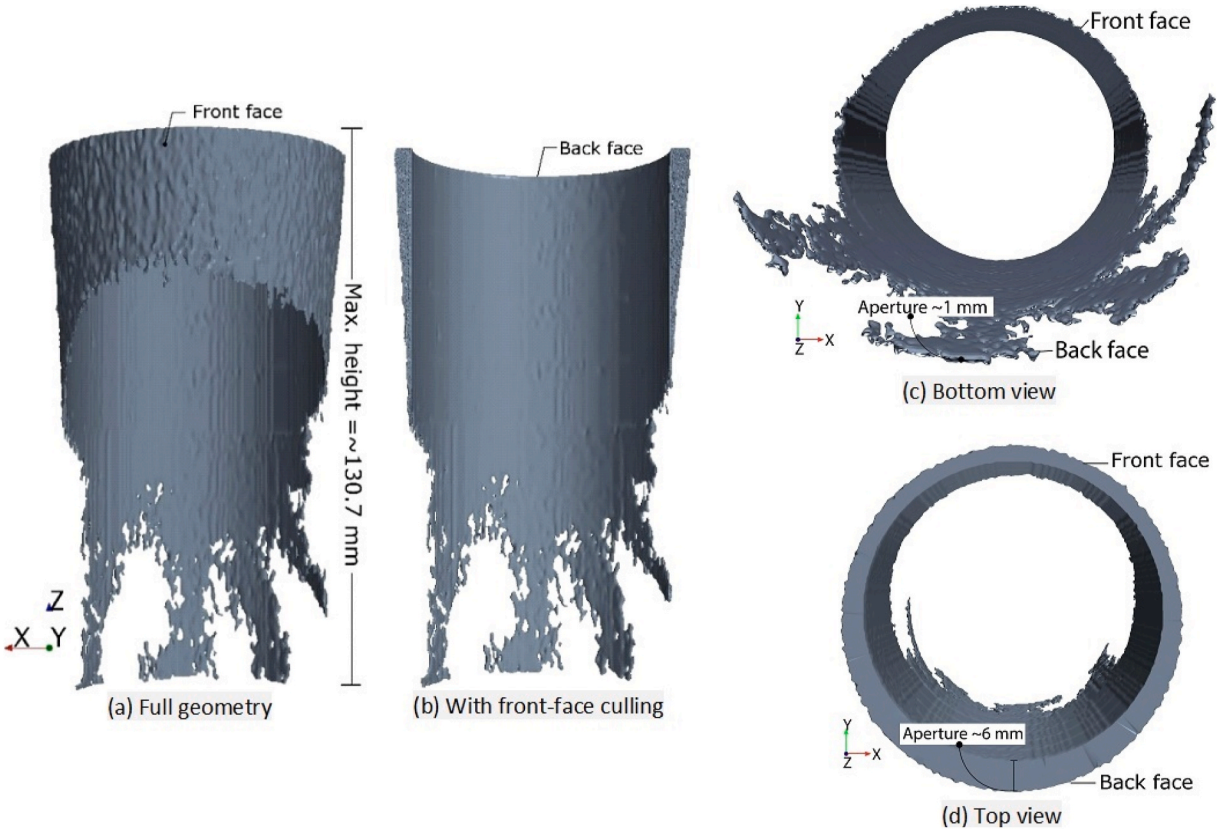

Fig. 3. Geometry of partial microannulus (Case 1), viewed from the front (a and b), the bottom (c), and the top (d).

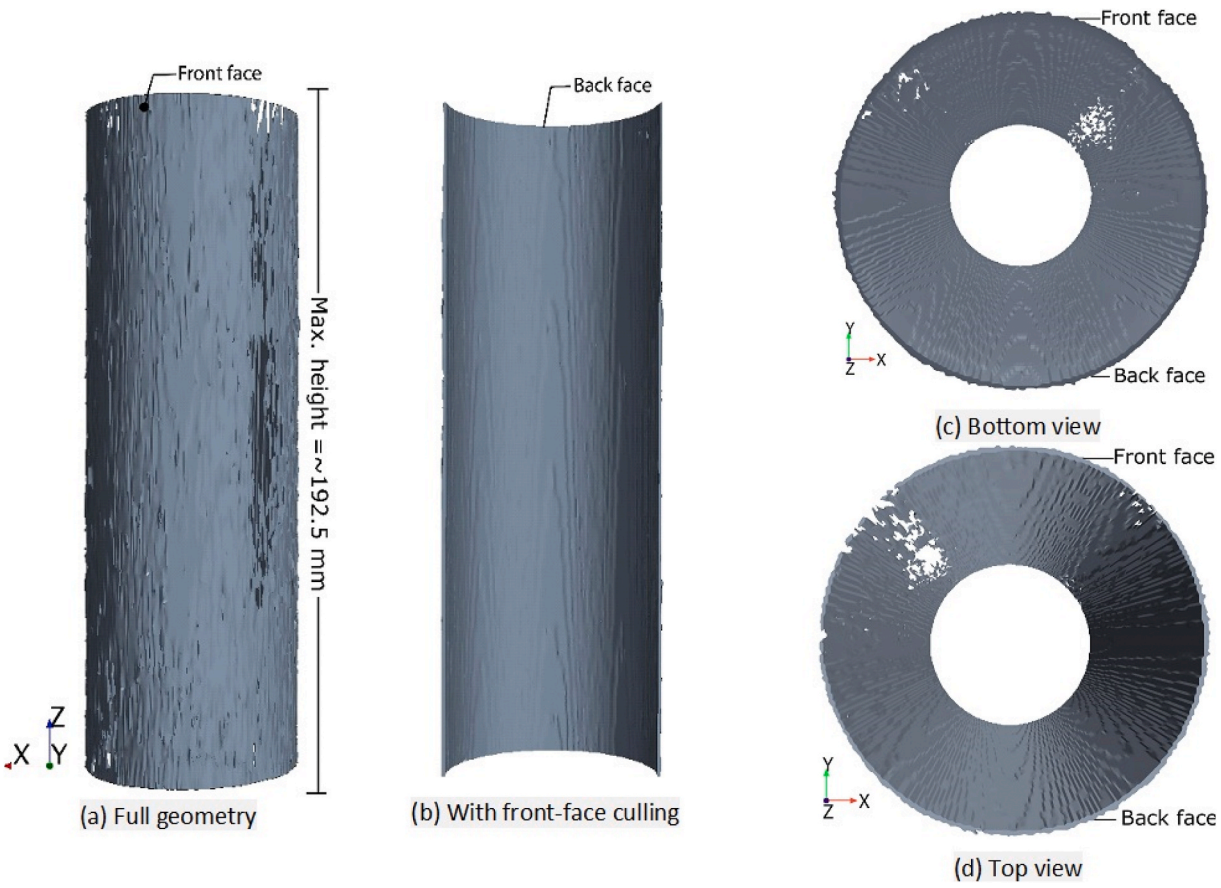

Fig. 4. Geometry of nearly complete microannulus (Case 2), viewed from the front (a and b), the bottom (c), and the top (d).

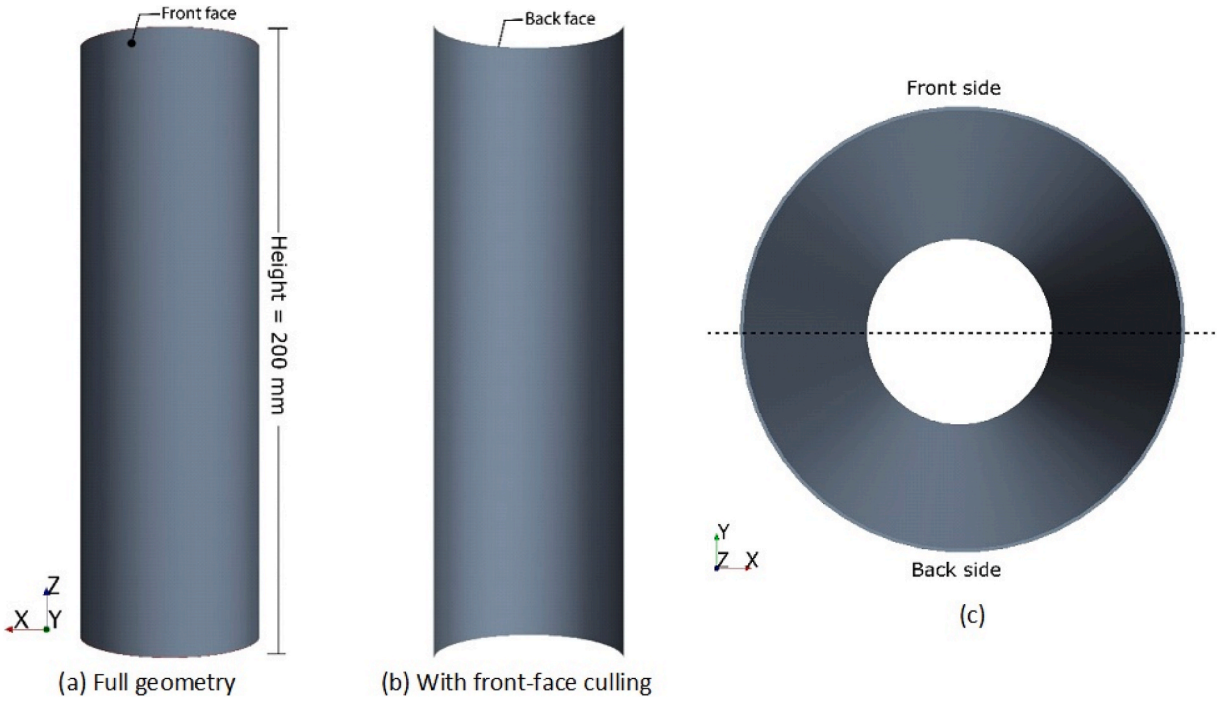

Fig. 5. Geometry of theoretical microannulus (50 μm), viewed from the front (a and b) and the top (c).

Table 1
Summary of the microannuli geometry cases.

Case #	Geometry	Description
Case 1	Experimental	Partial microannulus
Case 2	Experimental	Nearly complete microannulus
Case 3	Theoretical	Uniform aperture of 50 μm
Case 4	Theoretical	Uniform aperture of 350 μm
Case 5	Theoretical	Uniform aperture of 750 μm

Table 2
Density and viscosity of fluids used in the CFD simulations.

Fluid type	Density (kg/m^3)	Dynamic viscosity (Pa·s)
Methane gas	0.4911	14.09×10^{-6}
Water	940.7	2.25×10^{-4}
Oil	710	3.5×10^{-3}

that the microannulus aperture varied considerably around the circumference of the cement and concluded that microannuli have complex, non-uniform geometries. Consequently, they describe the difference between *mechanical aperture*, which is the actual distance across the microannulus opening, and the *hydraulic aperture*, which is the estimated, average aperture assuming flow through smooth-walled parallel plates (Stormont et al., 2018; Garcia et al., 2019; Hatambeigi et al., 2020).

Therefore, to better understand actual flow through real microannuli, it is important to take realistic microannuli geometries and resulting flow non-linearities into account. In this paper, we have expanded the previous work by Skorpa and Vrålstad (2018) and used new CT visualizations of experimentally created microannuli as imported geometries in CFD simulations of fluid flow. We have used these real microannuli geometries as flow paths for simulations with three different fluids: methane, water, and oil. For comparison, simulations with three different theoretical microannuli geometries with uniform apertures were performed as well. The objective is to visualize and understand how different fluids flow through real microannuli geometries, and such improved understanding will enable more accurate predictions of potential well leakage rates and thus contribute to improved well integrity.

2. Methodology

2.1. Preparation and visualization of microannuli

The microannuli geometries used in this paper were obtained from previously published work (De Andrade et al., 2016; Vrålstad et al., 2019), thus no new experiments were performed. The experimental procedure to obtain the microannuli have been described in detail in previous publications (De Andrade et al., 2014, 2016; Vrålstad et al., 2015; Vrålstad and Skorpa, 2020), and only a brief summary is given here:

Down-scaled cement sheaths were prepared experimentally, between a casing and a rock (Fig. 1) with a thickness of approx. 8 mm and a height of 200 mm. The casing (carbon steel, API 5 L X-52) has an outer diameter of 60.3 mm, surrounded by a cylindrical rock with an inner diameter of 76 mm and an outer diameter of 150 mm.

The casing/cement/rock specimens were mapped with X-ray computed tomography (CT) by using a Siemens Somatom Sensation medical CT scanner. The scanning process returned a stack of 200 sequential 2D cross-sectional images with a displacement of 1 mm/slice at 140 kV. The radial resolution of the CT scan was approximately 200 μm. The stack of the 2D images was processed and reconstructed to produce the 3D geometries by using the Avizo software (Thermo Fisher Scientific, 2019), as illustrated in Fig. 2. In the process, cement defects (dark areas) in the 2D-images were identified, where cement-casing debonding were labeled with blue color. At the end of the process, the 2D images were stacked to produce full 3D volumes of cement-casing microannuli. These 3D geometries were subsequently imported into the CFD simulation tool, as described in section 2.3.

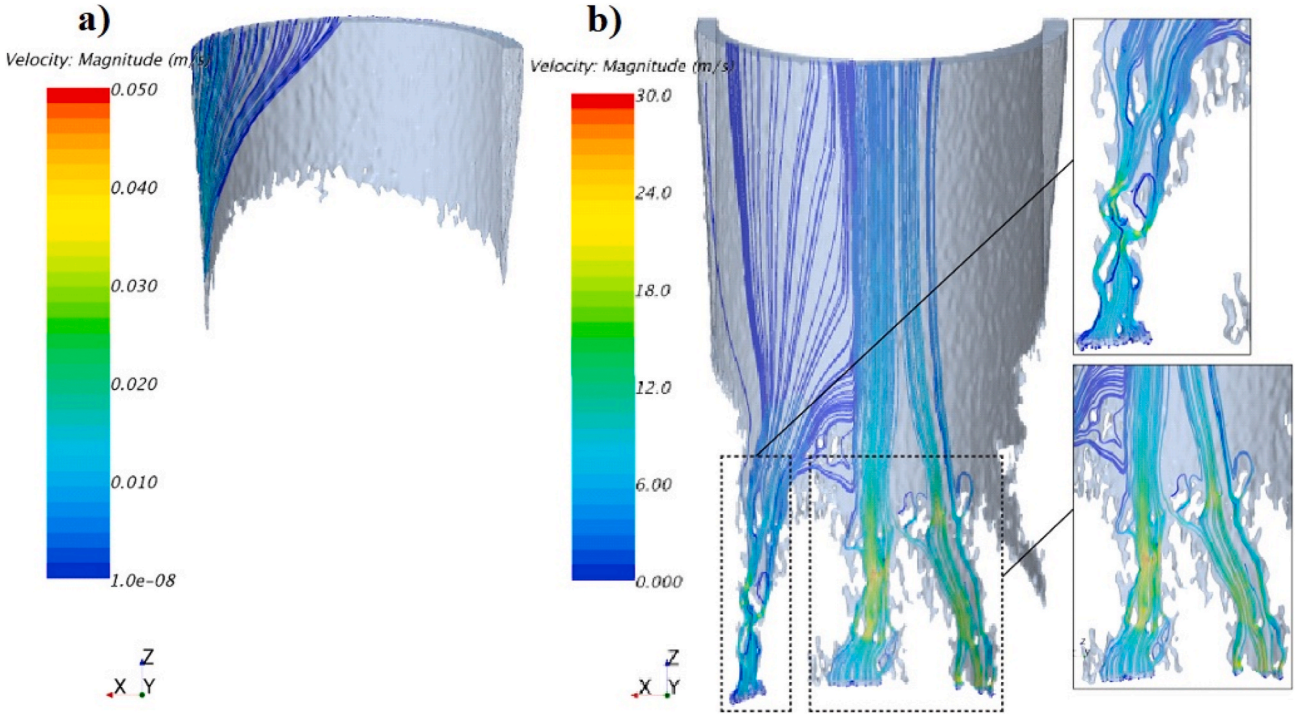

Fig. 6. Flow streamlines of methane gas at $\nabla P = 2.5$ kPa/m through the microannulus of Case 1 at (a) the front face and (b) the back face. Note that each microannulus face has a different range of fluid velocity.

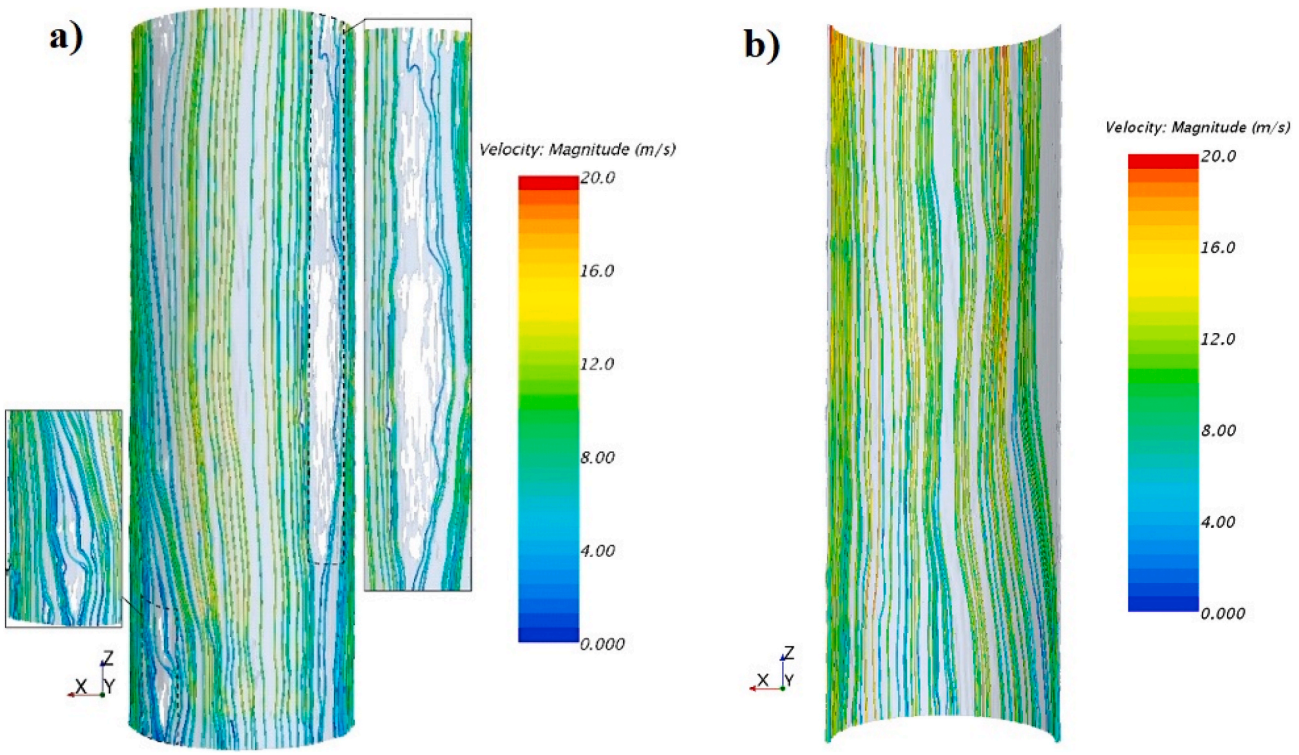

Fig. 7. Flow streamlines of methane gas at $\nabla P = 2.5$ kPa/m through the microannulus of Case 2 at (a) the front face and (b) the back face.

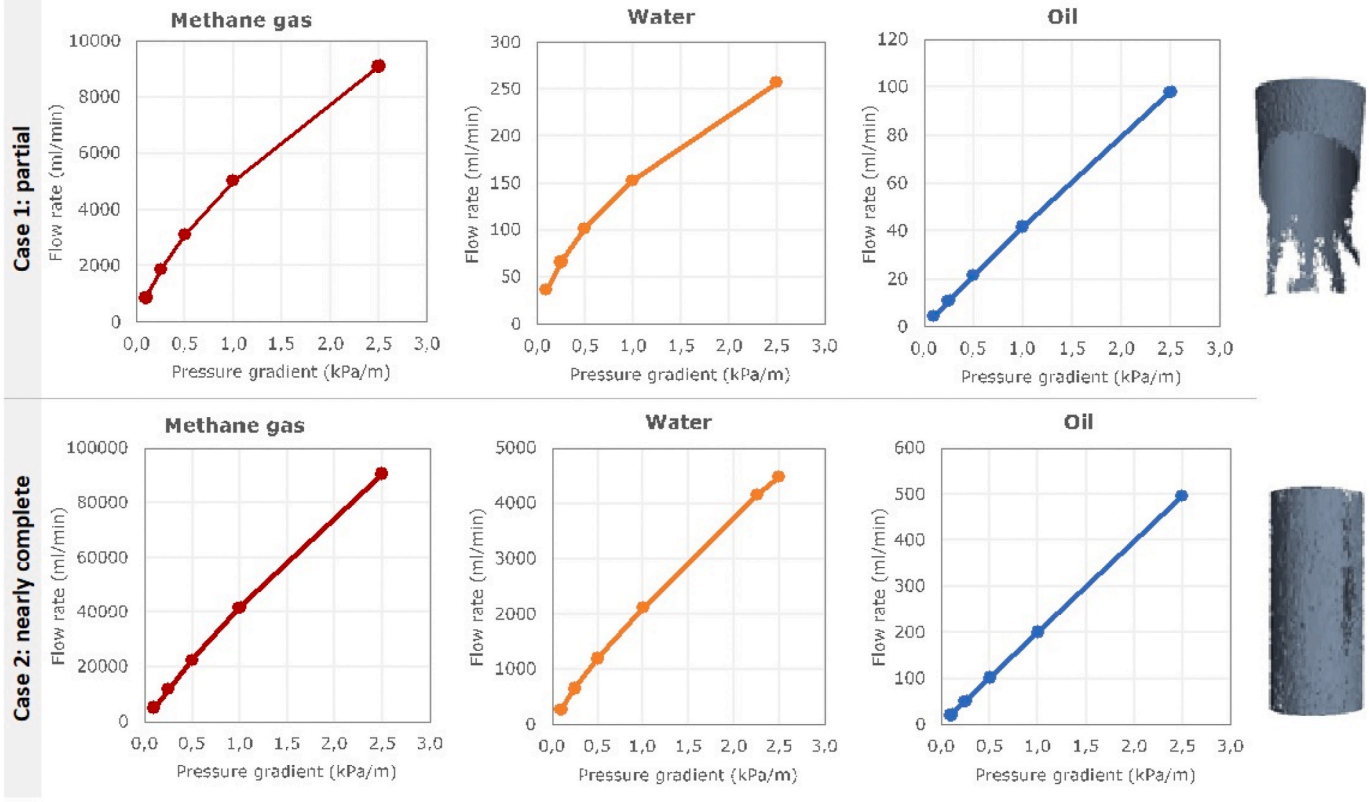

Fig. 8. CFD simulation results of pressure difference vs. flow rate for real microannuli geometries (Cases 1 and 2).

Table 3
Summary of the averaged Forchheimer number for all fluid types flowing through all microannulus geometries.

Geometry	Cases	Forchheimer number		
		Methane gas	Water	Oil
Experimental	Case 1	0.74[a]	2.17[†]	0.04
	Cas[a] 2	0.13[†)]	0.13[†]	0[a]01
Theoretical	Cas[a] 3	1×10^{-6}	3.7×10^{-3}	-1.5×10^{-4}[‡]
	Case 4	1.5×10^{-4}	0[b]01	3.3×10^{-5}
	Case 5	0.03	0.17[†]	7×10^{-4}

[†] Forchheim.
[‡] Negative sign indica.
[a] rnumbereaceeds the critical value of 0.11.
[b] es the flow is linear-Darcy flow dominant.

2.2. Description of microannuli geometries

Two experimentally obtained microannuli (Cases 1 and 2) were obtained from previous publications, where Case 1 has been shown by Vrålstad et al. (2019) and Case 2 has been shown by De Andrade et al. (2016). These two geometries were selected as examples of typical, real microannuli. For comparisons, three theoretical microannuli with uniform apertures were prepared as well.

Fig. 3 shows the geometry of Case 1, which is a partial microannulus. It is seen that casing-cement debonding dominates the area at the back face, and there was only partial microannulus present at the upper half of the front face. The microannulus at the back face is also vertically connected from the bottom to the top of the specimen. The microannulus aperture at the lower part is ~1 mm, and it increases along the z-direction and the circumference toward the back face, with the largest (~6 mm) found at the topmost of the back face. The volume of this microannulus is 35.87 mL.

Fig. 4 shows the geometry of Case 2, which is a nearly complete microannulus. It is seen that casing-cement debonding dominates the entire interface circumference and is also vertically connected from the bottom to the top of the specimen. There are only a few cement-casing contacts at the front face, and hence this microannulus nearly shapes a complete microannulus. The microannulus aperture is generally uniform at ~0.8 mm, and the volume of the microannulus is 32.95 mL.

In addition to these two experimental microannuli, three hypothetical microannuli (Cases 3–5) were prepared manually by using the CFD simulation software. They share a similar geometry of smooth and perfectly uniform thickness. Three different microannulus apertures were prepared: 50 μm (Fig. 5), 350 μm, and 750 μm. 50 μm was chosen to represent a typical value for average, hydraulic apertures found in experimental studies (Boukhelifa et al., 2004; Aas et al., 2016; Stormont et al., 2018), whereas 350 μm and 750 μm were chosen to approximately match the obtained simulation results for Cases 1 and 2, respectively. A summary of the geometry cases from both experimental and theoretical microannuli is given in Table 1.

2.3. Computational fluid dynamics (CFD) simulations

The procedure to perform the CFD simulations has been described in detail in previous publications (Vrålstad et al., 2015; Skorpa and Vrålstad, 2018, 2020), but a detailed description is given here as well, along with specific descriptions of the simulations in this work. The digitalized microannuli geometries, as illustrated in Figs. 3–5, was imported into the CFD simulation software, StarCCM+ (Siemens PLM Software 2017). Each surface was manually repaired to maintain the unique structural features and flow paths, and small/unconnected dead-ends were removed to simplify the model. The inlet and outlet were defined at the bottom and top of the geometries, respectively. A wall boundary was used for the full geometry, except at the inlet and outlet surfaces, which were set as pressure outlet. The volume mesh (approximately 10 million faces) was generated using a polyhedral (for Case 1) and trimmer mesh (Case 2 and theoretical microannuli) with 5 layers of prism mesh close to the wall. The trimmer mesh was chosen to speed up both the meshing and running process. To check the quality of the mesh, a mesh-convergence study was performed with different mesh

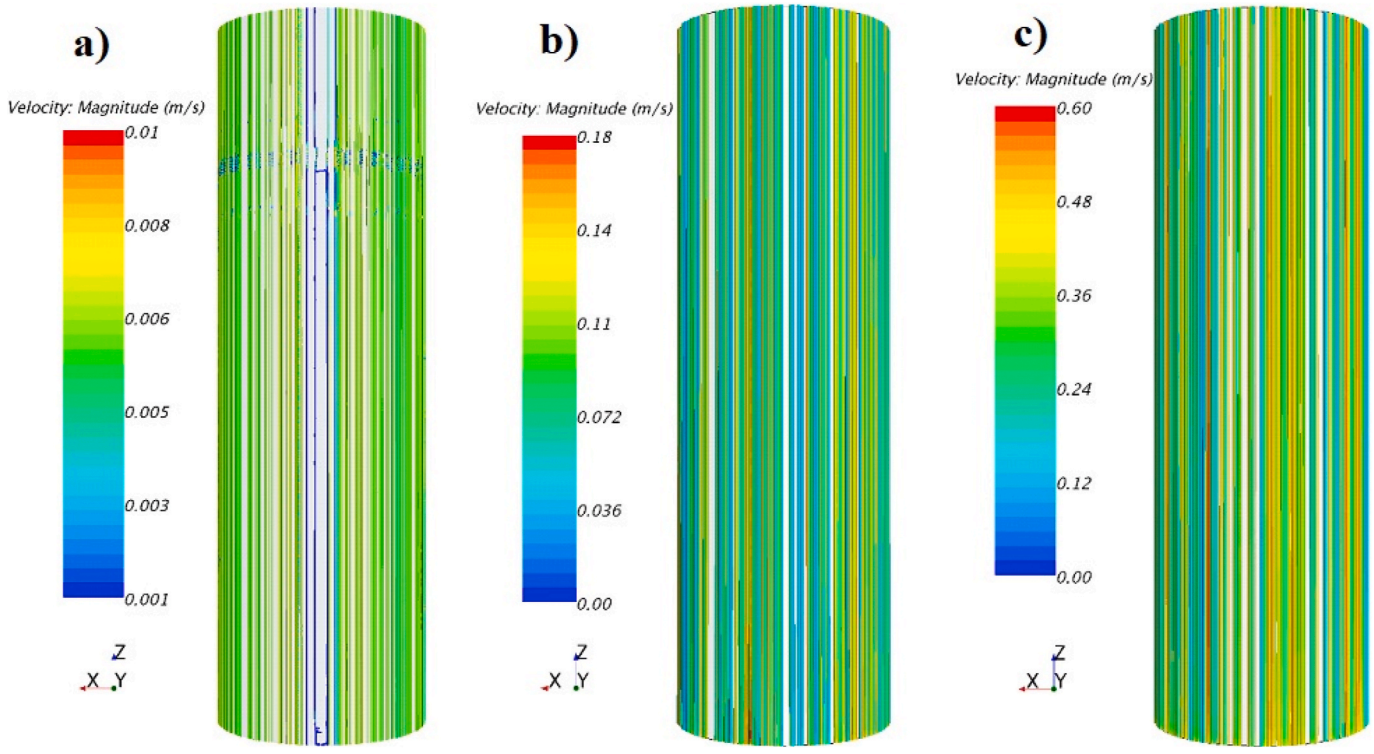

Fig. 9. The flow streamlines of water at $\nabla P = 2.5$ kPa/m through the microannulus of (a) Case 3, (b) Case 4, and (c) Case 5 at the front face. Note that each case has a different range of fluid velocity.

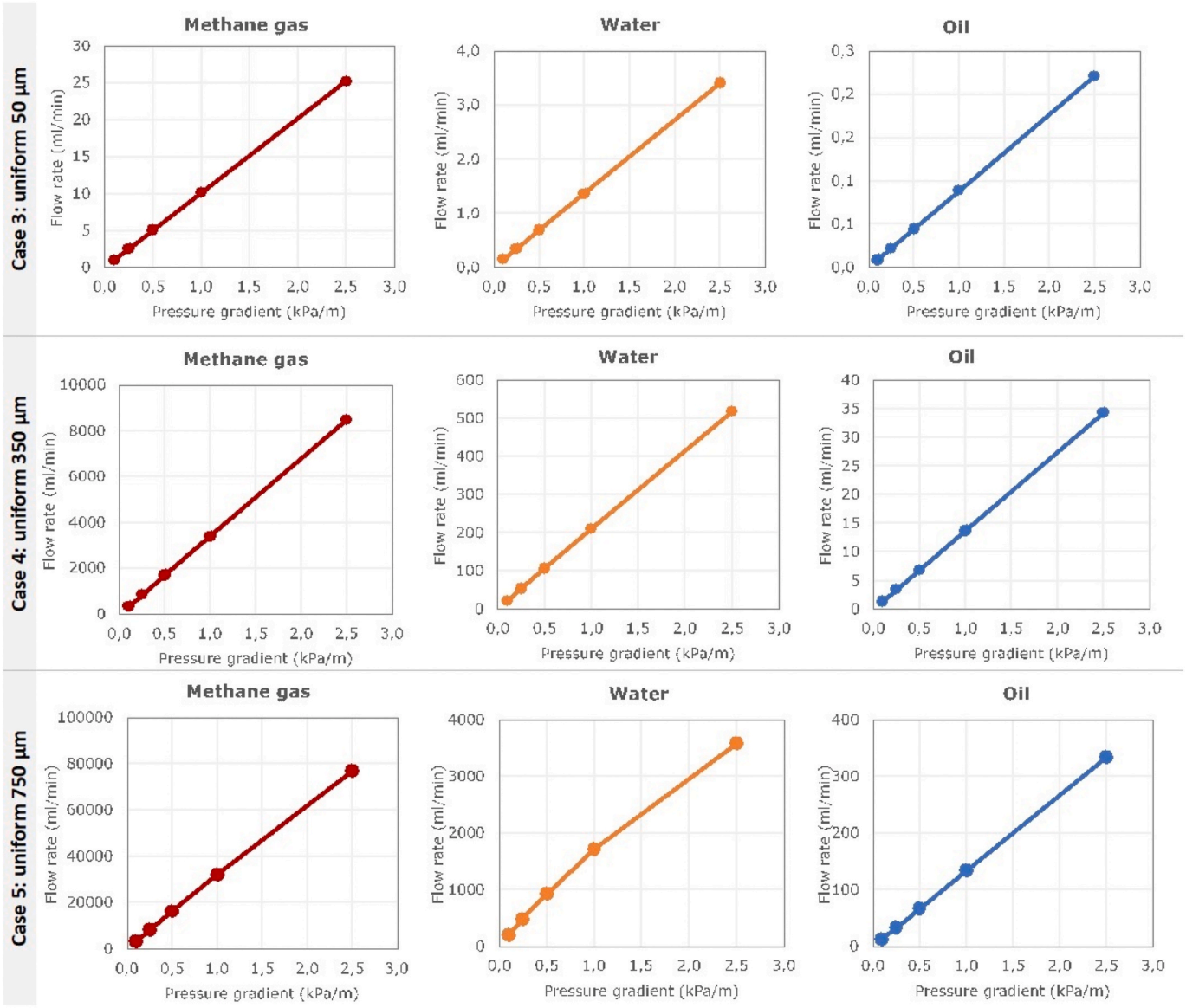

Fig. 10. CFD simulation results of pressure difference vs. flow rate for theoretical microannuli (Cases 3–5).

configurations and number of faces to check the quality of the mesh.

A mass flow through the geometry was created by applying a pressure at the bottom of the inlet, creating a pressure gradient (ranging from 0.1 to 2.5 kPa/m) through the geometry. The pressure at the outlet were fixed at 1 bar. The mass flow was modeled using segregated flow, constant density, and steady state approximations, assuming laminar flow through the geometry. Each simulation was run until numerical convergence of the residuals (approximately 3000 iterations), and both the mass flow and pressure drop were found to converge in due time before this. Three different fluids were investigated: methane (gas), water (liquid) and medium-light oil (liquid). The fluid properties, i.e. the density (ρ) and the dynamic viscosity (μ), were set at 120 °C and 1 bar and were obtained from the CFD software, as summarized in Table 2. It should be noted that for these values of pressure and temperature, it may seem peculiar that water should be in liquid state, however these fluid properties are representative for liquid water at elevated temperatures.

2.4. Non-linear fluid flow

Previous studies on fluid flow through microannuli and cracks in cement have shown that the flow do not follow Darcian linearity, but can be better explained by Forchheimer's equation for visco-inertial flow (Skorpa and Vrålstad, 2018, 2020; Stormont et al., 2018; Garcia et al., 2019; Hatambeigi et al., 2020). In Darcy flow, the flow rate is linearly related to the pressure gradient, and the relationship of both parameters is described by the following equation:

$$-\nabla P = \frac{\mu}{kA_h} Q \tag{1}$$

where ∇P is the pressure gradient along the flow direction (Pa/m), μ is the dynamic viscosity (Pa·s), k is the permeability (m^2), A_h is the cross-sectional area of the specimen (m^2), and Q is the volumetric flow rate (m^3/s).

Linear Darcy flow could be terminated and shifted into non-linear flow if the flow rate is a large or significant inertial effect emerged, i.e. an effect that is caused by the irreversible loss of kinetic energy due to flow acceleration or deceleration (Chen et al., 2015). To explain non-linear flow, Forchheimer (1901) added a quadratic term into the Darcy equation that represents the inertial effect, expressed as:

$$-\nabla P = AQ + BQ^2 \tag{2}$$

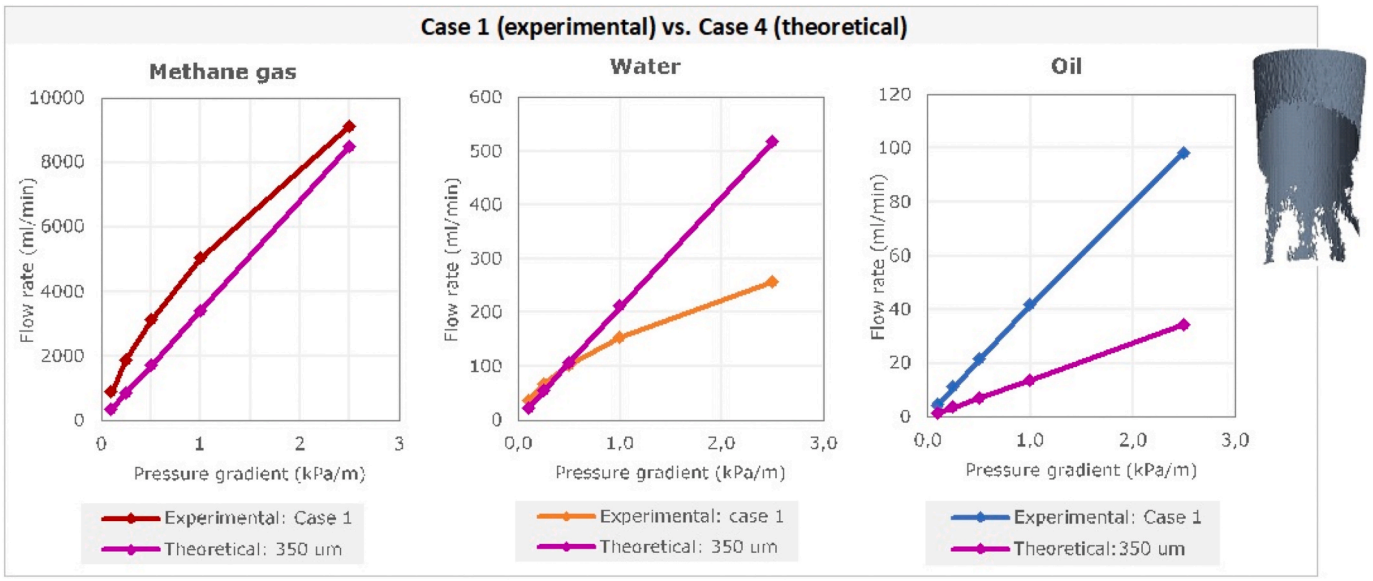

Fig. 11. Comparison of CFD simulation results between experimental Case 1 and theoretical Case 4.

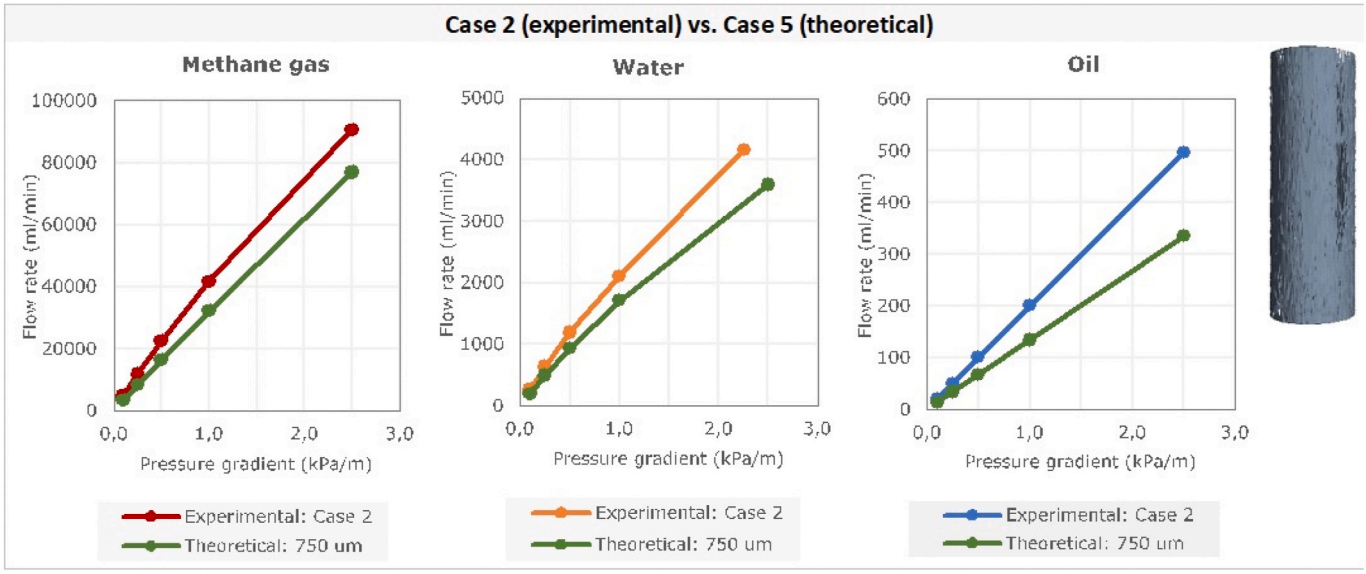

Fig. 12. Comparison of CFD simulation results between experimental Case 2 and theoretical Case 5.

$$-\nabla P = \frac{\mu}{kA_h} Q + \frac{\beta\rho}{A_h^2} Q^2 \tag{3}$$

where A and B are respectively the coefficients describing energy losses due to the viscous and inertial dissipation mechanisms, ρ is the fluid density (kg/m^3), and β is called the non-Darcy coefficient.

To accurately identify the type of fluid flow, the Forchheimer number is used to describe the criteria to enter non-Darcy flow. The Forchheimer number, F_0, is defined as the ratio of pressure gradient required to overcome inertial forces to that of viscous forces derived from Eq. (2) (Chen et al., 2015):

$$F_o = \frac{BQ^2}{AQ} = \frac{BQ}{A} \tag{4}$$

Zeng and Grigg (2006) suggested that 0.11 is the critical value of the Forchheimer number, where values of F_0 higher than 0.11 results in non-linear flow.

2.5. Limitations

There are several limitations in the procedure that affect the results, which should be discussed. The main limitation is the resolution of the CT instrument, which significantly influences the obtained microannuli geometries. Currently, the radial CT resolution is approx. 200 μm, which means that debonded areas smaller than this limit will not be detected. Consequently, the microannuli geometries obtained in our studies have relatively large apertures compared to other, experimental studies were microannuli have been found to be significantly smaller than 200 μm (Boukhelifa et al., 2004; (Nagelhout et al., 2010; Aas et al., 2016; Stormont et al., 2018; Garcia et al., 2019). Subsequently, the resulting flow rates obtained from our CFD simulations may be unrealistically high. However, the aim of this paper is to study and understand flow through real microannuli geometries, thus the obtained results are still qualitatively important.

Another limitation is that it is assumed that the microannuli

geometries are fixed and do not change during flow. This assumption is incorrect as it is known that increased pressure differences may lead to further cement debonding and thus increase the available flow path size (Bois et al., 2019). Furthermore, it is also assumed that fluid only flows through the microannuli, and not through the (porous) cement at all. However, the permeability of cement is relatively low, and flow through the cement can thus be neglected compared to microannuli flow.

3. Results and discussion

3.1. Experimental microannuli: case 1 and case 2

As examples of obtained simulation results, Figs. 6 and 7 show flow streamlines of methane gas flow at $\nabla P = 2.5$ kPa/m for Case 1 and Case 2, respectively. The fluid flow in the partial microannulus of Case 1 (Fig. 6) was mainly concentrated in the middle area of the back face, with parallel and straight flow streamlines and high velocity. This highway area, where fluid flows rapidly, was formed due to the highly connected microannulus with thick apertures (see Fig. 3c). Meanwhile, the flow at the neighboring area shifted into transverse streamlines toward the front face with velocity reduction. At the lower part of the back face, the fluid flow was tortuous with channeling streamlines along the preferential paths due to the non-uniform presence of cement-casing contacts. The local velocity of this flow was also highly varied, up to 30 m/s, which was likely due to the variation in the microannulus aperture.

The flow streamlines from the nearly complete microannulus of Case 2 (Fig. 7) were mainly homogeneous at both front and back faces, with wavy paralleled lines along the flow direction. However, near the area with irregular contact of cement-casing, a channeling flow was indicated (Fig. 7a). Furthermore, there were variations in fluid velocity along the flow direction, up to 20 m/s, although it was less significant than for Case 1.

Plots of pressure gradient versus resulting flow rate for each type of fluid for Cases 1 and 2 are presented in Fig. 8. It can be seen from the figure that non-linear curves are obtained for methane and water when flowing through both partial (Case 1) and nearly complete (Case 2) microannuli, whereas oil resulted in linear curves for both cases It is also observed that the non-linearity found for curves in Case 2 was less distinct than for Case 1, which is probably because Case 2 has a more uniform geometry than Case 1.

Furthermore, as mentioned in section 2.4, the Forchheimer equation can be used to describe non-linear flow through microannuli, where 0.11 is the critical value of the Forchheimer number (F_0) when the flow becomes non-linear (Zeng and Grigg, 2006). Table 3 summarizes the averaged F_o values for each case and fluid type. It can be seen from the table that in both Cases 1 and 2, large values of $F_o > 0.11$ were observed for methane gas and water, indicating non-linear flow. Moreover, values of $F_o < 0.11$ were found for oil, indicating linear flow, which verify the observations in Fig. 8. These findings suggest that inertial effects are more dominant in low viscous fluids, and that viscous effects are more dominant in more viscous fluids.

By comparing Cases 1 and 2, it can also be seen from Table 3 that the largest F_o values are found for the partial microannulus geometry of Case 1. These large F_o values suggest significant inertial effects, which could be attributed to (i) frequent flow acceleration or deceleration and (ii) a highly tortuous flow path (Chen et al., 2015; Zou et al., 2017). Both attributes were confirmed by the fluid streamlines observed for Case 1 in Fig. 6. Moreover, the less significant inertial effects, i.e. lower F_o values, observed for the nearly-complete microannulus geometry (Case 2), is reflected by the fluid streamlines in Fig. 7 that show mostly parallel flow paths with small velocity variations. Therefore, these findings suggest that flow linearity is highly dependent on microannuli morphology, where microannuli with more complex geometries increase the non-linearity of the fluid flow.

3.2. Theoretical microannuli: case 3 - case 5

As examples of obtained simulation results, Fig. 9 show flow streamlines of water flow in the theoretical microannulus of Cases 3–5 at $\nabla P = 2.5$ kPa/m. Overall, the streamlines in these three microannuli formed uniform and perfectly straight lines along the flow direction, with a small variation of fluid velocity. The range of the fluid velocity in each case increased as the aperture size increased. Plots of pressure gradient versus resulting flow rate for all fluids for the theoretical microannuli are presented in Fig. 10. It can be seen that fluid flow through all theoretical microannuli resulted in linear curves. However, the only exception was for water flow in the microannulus of Case 5, with the thickest aperture of 750 μm, which could perhaps be attributed to the high flow rates and the large density of water ($B \propto \rho$, see Equation (3)).

Table 3 shows that fluids in all theoretical models of Case 3–5 result in Forchheimer numbers less than 0.11, which verifies the observed linearity in Fig. 10, except for water flow in the largest aperture of 750 μm (Case 5) where $F_o > 0.11$. This observed linearity is expected as the flow path in these microannuli is uniform, with small variations of velocity (Fig. 9).

3.3. Comparison of experimental and theoretical microannuli

The results so far have confirmed and expanded previous findings by Skorpa and Vrålstad (2018), i.e. that fluid flow through microannuli is non-linear and that the degree of non-linearity increases with increasing microannuli non-uniformity. To elaborate this point further, it is fruitful to compare to results for experimental microannuli with theoretical microannuli. First, by comparing the results in Figs. 8 and 10, it is seen that the obtained flow rates for theoretical microannulus with 50 μm aperture (Case 3) are several orders of magnitude lower than the obtained flow rates for the two experimental cases. For direct comparisons, it is therefore more relevant to compare Cases 1 and 2 to Cases 4 and 5, respectively, which are shown in Figs. 11 and 12.

From Fig. 11 it can be seen that the results for uniform microannulus of Case 4 deviate significantly from the non-linear flow of methane gas and water seen for the real microannuli in Case 1. Similar deviations are also found for Case 2 vs Case 5 in Fig. 12, although less significant, since the microannulus geometry of Case 2 is more uniform than Case 1. Therefore, our findings indicate that it would be incorrect to assume uniform microannuli apertures and geometries when estimating flow through microannuli.

4. Conclusions

This study has demonstrated that fluid flow through microannuli is a complex issue, and the following conclusions can be drawn:

- Fluid flow in real microannuli can be non-linear due to the inhomogeneous and irregular morphology of the flow paths.
- The non-linearity of fluid flow in real microannuli increases as the microannuli geometries become more complex and heterogeneous.
- The Forchheimer number can be used to describe linear vs non-linear flow, where the value 0.11 predicts the transition from linear to non-linear.

Declaration of competing interest

The authors declare that they have no known competing financial interests or personal relationships that could have appeared to influence the work reported in this paper.

Acknowledgments

The authors would like to thank the Research Council of Norway,

Aker BP, ConocoPhillips, Equinor, and Wintershall for financing the work through the research center DrillWell.

Appendix A. Supplementary data

Supplementary data to this article can be found online at https://doi.org/10.1016/j.petrol.2020.107669.

References

Aas, Bjarne, Sørbø, Jostein, Stokka, Sigmund, et al., 2016. Cement placement with tubing left in hole during plug and abandonment operations. In: Presented at the IADC/SPE Drilling Conference and Exhibition. https://doi.org/10.2118/178840-MS. Fort Worth, Texas, USA. 2016/3/1/.

Bachu, Stefan, Bennion, D. Brant, 2009. Experimental assessment of brine and/or CO2 leakage through well cements at reservoir conditions. Int. J. Greenh. Gas Contr. 3 (4), 494–501. http://www.sciencedirect.com/science/article/pii/S1750583608001035.

Bois, Axel-Pierre, Garnier, Andre, Rodot, Francois, et al., 2011. How to prevent loss of zonal isolation through a comprehensive analysis of microannulus formation, 01 SPE Drill. Complet. 26, 13–31.

Vu, Manh-Huyen, Bois, Axel-Pierre, Noël, Kim, et al., 2019. Evaluating cement-plug mechanical and hydraulic integrity. SPE Drill. Complet. 34, 92–102. https://doi.org/10.2118/191335-PA (02).

Boukhelifa, L., Moroni, N., James, S.G., et al., 2004. Evaluation of cement systems for oil and gas well zonal isolation in a full-scale Annular geometry. In: Presented at the IADC/SPE Drilling Conference. https://doi.org/10.2118/87195-MS. Dallas, Texas. 2004/1/1/.

Bourgoyne, A.T., Scott, S.L., Regg, J.B., 1999. Sustained casing pressure in offshore producing wells. Paper OTC-11029. In: Presented at the Offshore Technology Conference Held in Houston. Texas, USA, 3-6 May 1999.

Chen, Yi-Feng, Zhou, Jia-Qing, Hu, Shao-Hua, et al., 2015. Evaluation of forchheimer equation coefficients for non-Darcy flow in deformable rough-walled fractures. J. Hydrol. 529, 993–1006. http://www.sciencedirect.com/science/article/pii/S0022169415007040.

Corina, A.N., Opedal, N., Vrålstad, T., Skorpa, R., Sangesland, S., 2020. The Effect of Casing Pipe Roughness on Cement Plug Integrity. SPE Drilling & Completion. Paper SPE-194158-PA.

De Andrade, J., Torsaeter, M., Todorovic, J., et al., 2014. Influence of casing centralization on cement sheath integrity during thermal cycling. In: Presented at the IADC/SPE Drilling Conference and Exhibition. https://doi.org/10.2118/168012-MS. Fort Worth, Texas, USA. 2014/3/4/.

De Andrade, Jesus, Sangesland, Sigbjorn, Skorpa, Ragnhild, et al., 2016. Experimental laboratory setup for visualization and quantification of cement-sheath integrity, 04 SPE Drill. Complet. 31, 317–326. https://doi.org/10.2118/173871-PA.

Duguid, Andrew, Butsch, Robert, Carey, J. William, et al., 2013. Pre-injection baseline data collection to establish existing wellbore leakage properties. Energy Procedia 37, 5661–5672. http://www.sciencedirect.com/science/article/pii/S1876610213007315.

Thermo Fisher Scientific, 2019. Avizo software for materials research: materials characterization and quality control (reprint). https://assets.thermofisher.com/TFS-Assets/MSD/brochures/brochure-avizo-software-materials-research.pdf.

Forchheimer, P., 1901. Wasserbewegung durch Boden. Zeitz ver Deutsch Ing 45, 1782–1788.

Ford, E., Moeinikia, F., Majourmerd, M.M., Lohne, H.P., Arild, Ø., 2018. Consequence Quantification of Barrier System Failures in Permanently Plugged and Abandoned Wells. Paper SPE-191298-MS Presented at the SPE Norway One Day Seminar Held in Bergen. Norway 18 April 2018.

Garcia, Fernandez, Serafin, Matteo, Edward, N., Taha, Mahmoud Reda, et al., 2019. Characterization of wellbore microannuli. J. Nat. Gas Sci. Eng. 62, 13–25. http://www.sciencedirect.com/science/article/pii/S1875510018305316.

Gasda, Sarah E., Celia, Michael A., Wang, James Z., et al., 2013. Wellbore permeability estimates from vertical interference testing of existing wells. Energy Procedia 37, 5673–5680. http://www.sciencedirect.com/science/article/pii/S1876610213007327.

Hatambeigi, M., Chojnicki, K., Taha, M.R., Stormont, J.C., 2020. Visco-inertial gas flow through wellbore cement fractures. J. Nat. Gas Sci. Eng. 77, 103275.

Moeinikia, F., Ford, E., Lohne, H.P., Arild, Ø., Majourmerd, M.M., Fjelde, K.K., 2018. Leakage calculator for plugged-and-abandoned wells, 04 SPE Prod. Oper. 33, 790–801. SPE-185890-PA.

Nagelhout, Alexander, Bosma, Martin G.R., Mul, Paul, et al., 2010. Laboratory and field validation of a sealant system for critical plug-and-abandon applications. SPE Drill. Complet. 25, 314–321. https://doi.org/10.2118/97347-PA (03).

Nelson, E.B., Guillot, D., 2006. Well Cementing. Schlumberger, second ed. (Sugarland, Texas).

Nygaard, R., Salehi, S., Weideman, B., Lavoie, R., 2014. Effect of dynamic loading on wellbore leakage for the wabamun area CO2-sequestration project. J. Can. Petrol. Technol. 53 (01), SPE-146640-PA.

Oil, Gas, U.K., 2015. Guidelines on Qualification of Materials for the Abandonment of Wells. Oil & Gas UK, Great Britain. Issue 2.

Skorpa, R., Vrålstad, T., 2018. Visualization of fluid flow through cracks and microannuli in cement sheaths. SPE J. 23, 04.

Skorpa, R., Vrålstad, T., 2020. Leakages through radial cracks in cement sheaths: effect of geometry, viscosity and aperture. In: Paper OMAE2020-18496 Presented at the ASME 2020 39th International Conference on Ocean, Offshore and Arctic Engineering. June 28 – July 3, 2020, Fort Lauderdale, FL, USA.

Stormont, John C., Fernandez, Serafin Garcia, Taha, Mahmoud R., et al., 2018. Gas flow through cement-casing microannuli under varying stress conditions. Geomech. Energy Environ. 13, 1–13. http://www.sciencedirect.com/science/article/pii/S2352380817300436.

Therond, E., Bois, A.-P., Whaley, K., Murillo, R., 2017. Large-scale testing and modeling for cement zonal isolation in water-injection wells. SPE Drill. Complet. 32 (04), SPE-181428-PA.

Trudel, E., Bizhani, M., Zare, M., Frigaard, I., 2019. Plug and abandonment practices and trends: a British Colombia perspective. J. Petrol. Sci. Eng. 183, 106417.

Vignes, B., Aadnoy, B., 2010. Well integrity issues offshore Norway. SPE Prod. Oper. 25 (02), SPE-112535-PA.

Vrålstad, T., Skorpa, R., 2020. Digital cement integrity: a methodology for 3D visualization of cracks and microannuli in well cement. Sustainability 12, 4128.

Vrålstad, Torbjørn, Skorpa, Ragnhild, Opedal, Nils, et al., 2015. Effect of thermal cycling on cement sheath integrity: realistic experimental tests and simulation of resulting leakages. In: Presented at the SPE Thermal Well Integrity and Design Symposium. Banff, Alberta, Canada. https://doi.org/10.2118/178467-MS, 2015/11/23/.

Vrålstad, Torbjørn, Saasen, Arild, Fjær, Erling, et al., 2019. Plug & abandonment of offshore wells: ensuring long-term well integrity and cost-efficiency. J. Petrol. Sci. Eng. 173, 478–491. http://www.sciencedirect.com/science/article/pii/S0920410518309173.

Watson, T.L., Bachu, S., 2009. Evaluation of the potential for gas and CO2 leakage along wellbores, 01 SPE Drill. Complet. (24) Paper SPE-106817-PA.

Zeng, Z., Grigg, R., 2006. A criterion for non-Darcy flow in porous media. Transport Porous Media 63 (1), 57–69. https://doi.org/10.1007/s11242-005-2720-3.

Zou, Liangchao, Jing, Lanru, Cvetkovic, Vladimir, 2017. Shear-enhanced nonlinear flow in rough-walled rock fractures. Int. J. Rock Mech. Min. Sci. 97, 33–45. http://www.sciencedirect.com/science/article/pii/S1365160917306810.

PLM Software, 2017. Star-CCM+ (Reprint). https://mdx.plm.automation.siemens.com/star-ccm-plus.